ANZIAM J. **68, e19** (2026), 1–19
doi:10.1017/S144618112610042X

BULK FLUX FOR WAVY CHANNEL STOKES FLOW

STEPHEN J. WALTERS[1] and LAWRENCE K. FORBES[1]

(Received 17 March, 2026 UTC; accepted 8 June, 2026 UTC)

Abstract

Calculation of the flux through a two-dimensional channel with one sinusoidal wall is presented using a perturbation expansion. This gives a series for the flux up to $O(\epsilon^{160})$, where ϵ is the amplitude of the wall undulation, ranging from 0 (flat wall) to 2 (channel pinched off). The series appears to diverge near $\epsilon = 0.95$, but is continued through the use of Padé approximants. The divergence is investigated and found to be caused by pole singularities lying at $\epsilon \approx \pm 0.977i$ on the imaginary axis. The continued series is validated against a purely numerical solution with excellent agreement for all values of the undulation amplitude.

2020 *Mathematics subject classification*: 76M45.

Keywords and phrases: Perturbation series, asymptotic methods, viscous fluid flow, numerical methods, spectral methods.

1. Introduction

Viscous flows in channels with irregular walls occur across a range of physical scenarios, and represent an important and ongoing area of research. These flows are mathematically complicated, and various simplifications and approximations have been used and are being developed. The first obvious simplification is to ignore inertial terms when considering low Reynolds number flows, which occur for very viscous or slow-moving flows. This is the so-called Stokes regime, which reduces the Navier–Stokes equations to a linear system.

Lubrication is such an important feature of modern machinery that its properties have been extensively studied at least since the 1886 paper by Reynolds [8]. Applications vary widely, ranging from machine bearings [10] to peristaltic motion [3] and blood flow [5]. Of the many papers on this topic, a few closely related papers are

[1]Mathematics Department, School of Natural Sciences, University of Tasmania, Tasmania 7005, Australia; e-mail: stephen.walters@utas.edu.au, larry.forbes@utas.edu.au
© The Author(s), 2026. Published by Cambridge University Press on behalf of The Australian Mathematical Publishing Association Inc. This is an Open Access article, distributed under the terms of the Creative Commons Attribution licence (https://creativecommons.org/licenses/by/4.0), which permits unrestricted re-use, distribution and reproduction, provided the original article is properly cited.

https://doi.org/10.1017/S144618112610042X Published online by Cambridge University Press

highlighted here. Sobey [11] used numerical solutions of the Navier–Stokes equations to characterise steady and oscillatory flow patterns in a furrowed channel modelled on a contemporary blood oxygenator design, identifying the critical Reynolds number for flow separation. Tsangaris and Leiter [12] performed a first-order analytical perturbation expansion for flow in sinusoidal channels, somewhat similar to our approach here. They also provide a good coverage of the literature up to that point in their introduction.

In a different approach, Pozrikidis [7] considered Stokes flow through two- dimensional (2D) channels using an integral boundary method. A three-dimensional study for wavy-wall flow was undertaken by Malevich *et al.* [6], considering the development of eddies in the flow. Standard lubrication theory is most commonly used in estimating flux through a channel. It assumes the Stokes regime, and also that the channel height is small relative to the wavelength. Refinements involving a series expansion in the slope of the channel undulations out to the fourth power have been performed by Tavakol *et al.* [13].

As an alternative approach in the current paper, while we still assume the Stokes regime, we do not assume that the wavelength is large relative to the channel height. Instead we implement a traditional perturbation expansion using the amplitude of the wall undulation as the small parameter ϵ. Stokes flow here presents a homogeneous biharmonic equation to solve for each mode at each order. However, each of these equations may be solved in coefficient space, and involve just two coefficients per mode at each order. The low cost and high accuracy of the expansion allows calculations out to $O(\epsilon^{160})$ in the undulation amplitude ϵ. The result is a highly efficient method for computing the flux through the channel for any perturbation height.

The expansion is continued past its radius of convergence with the use of Padé approximants, and validated carefully using our more general numerical method [15]. An analysis of the Domb–Sykes plot and the Padé denominators is explored in order to determine the nature and location of the singularity underlying the divergence of the perturbation expansion series. This gives unique insight into the mathematical structure of the solution, up to and including the physical limit $\epsilon = 2$.

The paper is structured as follows. In Section 2, a description and algorithm for the perturbation expansion is given, and Section 3 provides details of the numerical method used to validate the results. Section 4 presents a comparison of these results, using Padé approximants and a Domb–Sykes analysis [4] of the coefficients, and some concluding remarks are made in Section 5.

2. Two-dimensional Stokes flow: perturbation expansion

We consider incompressible steady Stokes flow of a viscous fluid in two dimensions, with gravitational body force along the channel. The problem is described by the continuity equation, and the Navier–Stokes equation with the convective terms removed. The system is nondimensionalised using the channel half-height H and other scalings as given in our recent paper [15]. The upper wall is a flat surface located at

https://doi.org/10.1017/S144618112610042X Published online by Cambridge University Press

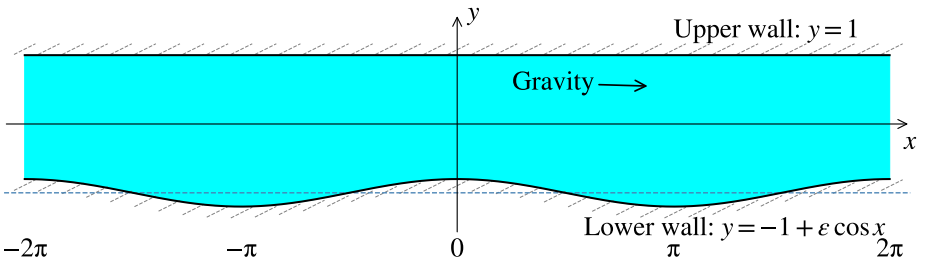


FIGURE 1. A schematic of the 2D channel with $-1+\epsilon\cos x < y < 1$ and π-periodic in x. Gravity points along the channel in the $+x$ direction.

$y = 1$, but the lower wall has a sinusoidal shape $f(x)$ with dimensionless period 2π and amplitude ϵ, and is centred at $y = -1$. In this paper we choose $f(x) = \cos x$. A sketch of the dimensionless channel configuration is given in Figure 1. For convenience, we choose the channel to have aspect ratio π (wall wavelength over channel width), but generalisation to different ratios is straightforward, and is pursued at the end of Section 4.

In 2D flow, there are two velocity components u and v, and P denotes pressure. Conservation of mass requires

$$u_x + v_y = 0,$$

and the two components of the linearised Navier–Stokes equation, appropriate for slow Stokes flow of a viscous fluid, are

$$u_{xx} + u_{yy} = P_x - 2, \tag{2.1}$$
$$v_{xx} + v_{yy} = P_y. \tag{2.2}$$

The viscous no-slip boundary condition on the upper wall in Figure 1 is simply

$$u = 0, v = 0 \quad \text{on } y = 1,$$

and on the lower wall

$$u = 0, v = 0 \quad \text{on } y = -1 + \epsilon\cos x.$$

Notice that the gravitational body force along the channel is chosen to be 2 in our nondimensionalisation, to give the simple form (2.5) for the Poiseuille profile. This body force term is also equivalent to an applied mean pressure gradient $dP/dx = -2$.

This system is now subjected to a perturbation expansion in the small parameter ϵ, which is the amplitude of the lower wall function:

$$\begin{aligned} u &= u_0 + \epsilon u_1 + \epsilon^2 u_2 + \cdots, \\ v &= v_0 + \epsilon v_1 + \epsilon^2 v_2 + \cdots, \\ P &= P_0 + \epsilon P_1 + \epsilon^2 P_2 + \cdots. \end{aligned} \tag{2.3}$$

https://doi.org/10.1017/S144618112610042X Published online by Cambridge University Press

The lower boundary conditions also must be expanded in terms of ϵ:

$$\begin{aligned} &u(x,-1+\epsilon\cos x)=0,\\ &u_0(x,-1)+\epsilon u_1(x,-1)+\epsilon\cos x\frac{\partial u_0}{\partial y}(x,-1)+\cdots=0, \end{aligned} \tag{2.4}$$

and similarly for v. The upper boundary conditions are simply $0 = u_n = v_n$ on $y = 1$ at every order n.

Applying the zeroth-order boundary conditions, $u = v = 0$ on $y = -1$, the zeroth-order solution is straightforward, yielding the parabolic profile flow

$$\begin{aligned} u_0&=1-y^2,\\ v_0&=0,\\ P_0&=0. \end{aligned} \tag{2.5}$$

Matching terms at $O(\epsilon)$, the first-order system is

$$\begin{aligned} u_{1,x}+v_{1,y}&=0,\\ u_{1,xx}+u_{1,yy}&=P_{1,x},\\ v_{1,xx}+v_{1,yy}&=P_{1,y}, \end{aligned}$$

with lower boundary conditions from (2.4):

$$\begin{aligned} u_1(x,-1)&=-2\cos x,\\ v_1(x,-1)&=0. \end{aligned} \tag{2.6}$$

The continuity equation may be satisfied in the usual way, by defining velocity components at each order in terms of a stream function ψ, such that

$$u_n=\frac{\partial\psi_n}{\partial y},\quad v_n=-\frac{\partial\psi_n}{\partial x}.$$

Then, subtracting the x-derivative of (2.2) from the y-derivative of (2.1), we arrive at the biharmonic equation

$$\frac{\partial^4\psi_n}{\partial x^4}+2\frac{\partial^4\psi_n}{\partial x^2\partial y^2}+\frac{\partial^4\psi_n}{\partial y^4}=0,$$

subject to $u_n = v_n = 0$ on $y = 1$ (these top wall boundary conditions are zero for every mode m at each order n),with u_n and v_n specified on $y = -1$. At each order n, we isolate each mode m such that $u_n = \sum_m U_{n,m}$, $v_n = \sum_m V_{n,m}$, and we write the solution as

$$\begin{aligned} U_{n,m}&=\cos(mx)F_{n,m}(y),\\ V_{n,m}&=\sin(mx)G_{n,m}(y), \end{aligned}$$

where $G'_{n,m} = mF_{n,m}$ to satisfy continuity. That is, $\psi_{n,m} = \cos(mx)G_{n,m}(y)/m$, $m > 0$. Incorporating the top wall boundary conditions, we may write a general solution for $F_{n,m}$ and $G_{n,m}$ in the forms

https://doi.org/10.1017/S144618112610042X Published online by Cambridge University Press

$$\begin{aligned} F_{n,m} &= (mA_{n,m}(1-y)\cosh[m(1-y)] \\ &\quad + (A_{n,m} + B_{n,m}(1-y))\sinh[m(1-y)])/\cosh(2m), \\ G_{n,m} &= (-B_{n,m}(1-y)\cosh[m(1-y)] \\ &\quad + (B_{n,m}/m - mA_{n,m}(1-y))\sinh[m(1-y)])/\cosh(2m), \end{aligned} \tag{2.7}$$

where the constants $A_{n,m}$ and $B_{n,m}$ are determined from the boundary conditions for $U_{n,m}, V_{n,m}$ on $y = -1$. The constant denominator term is included to improve numerical stability.

To illustrate the procedure, we first solve for u_1. On $y = -1$, we have $u_1 = -2\cos(x)$, as in (2.6). We therefore look for a solution $u_1(x, y) = \cos(x)F_1(y)$, leading to

$$F_1^{IV} - 2F_1^{II} + F_1 = 0.$$

Using the general solution and applying the lower boundary conditions (2.6), we find

$$\begin{aligned} A_{1,1} &= \frac{\sinh(4) - 4\cosh^2(2)}{4 - \sinh^2(2)}, \\ B_{1,1} &= \frac{2\sinh(4)}{4 - \sinh^2(2)}. \end{aligned} \tag{2.8}$$

These constants define u_1 and v_1, noting that only the single mode $m = 1$ is nonzero.

Now the bulk flux through the channel may be calculated at any x, by integrating u from bottom to top. The bulk flux should be independent of x. This provides a useful check for the algorithm, where we can examine the flux at each cosine mode, to confirm that for $m > 0$, the flux at that mode is zero:

$$Q = \int_{y=f(x)}^{y=1} u\,dy. \tag{2.9}$$

Suppose that $q(y) = \int u\,dy$ is an antiderivative of the velocity component u. Then

$$\begin{aligned} Q &= q(1) - q(-1 + \epsilon\cos(x)) \\ &= \int_{-1}^{1} u_0\,dy + \epsilon\int_{-1}^{1} u_1\,dy - \epsilon\cos(x)u_0(x,-1) + O(\epsilon^2). \end{aligned} \tag{2.10}$$

Therefore at zeroth order, the contribution to the flux in (2.9) is

$$Q_0 = \int_{-1}^{1} u_0\,dy = 4/3.$$

At first order, the ϵ^1 terms in (2.10) evaluate to zero, so the first-order contribution to the flux is zero ($Q_1 = 0$).

https://doi.org/10.1017/S144618112610042X Published online by Cambridge University Press

Employing the coefficients $A_{1,1}, B_{1,1}$ from (2.8) in the general form (2.7), the velocity components at first order are

$$u_1 = \cos x[A_{1,1}(1-y)\cosh(1-y) + (A_{1,1} + B_{1,1}(1-y))\sinh(1-y)]/\cosh(2),$$
$$v_1 = \sin x[-B_{1,1}(1-y)\cosh(1-y) + (B_{1,1} - A_{1,1}(1-y))\sinh(1-y)]/\cosh(2).$$

By taking the y-derivative (signified using prime notation), and setting $y = -1$, on simplification we obtain derivatives on the lower boundary (for the next order calculations)

$$u_1'|_{-1} = \frac{4(-1 - 8e^4 + e^8)\cos(x)}{1 - 18e^4 + e^8},$$
$$v_1'|_{-1} = 2\sin(x).$$

At second order, the boundary conditions on $y = -1$ are

$$\begin{aligned} u_2 &= -fu_1' - \frac{f^2}{2}u_0'' \\ &= -\cos^2(x)\left(\frac{4(-1 - 8e^4 + e^8)}{1 - 18e^4 + e^8} - 1\right), \\ v_2 &= -fv_1' = -2\sin(x)\cos(x) = -\sin(2x), \end{aligned}$$

where $f(x) = \cos(x)$ is the lower boundary function. Since the boundary condition for u_2 involves the function $\cos^2(x) = \frac{1}{2} + \frac{1}{2}\cos(2x)$, u_2 is expected to involve both a zeroth- and a second-order mode in x. Therefore we make the ansatz

$$u_2 = U_{2,0} + U_{2,2}\cos(2x),$$
$$v_2 = V_{2,2}\sin(2x).$$

Look at the mean component $U_{2,0}$. The steady Stokes equations give

$$\partial_{yy}U_{2,0} = \partial_x P_{2,0} = 0,$$

so the zero mode is a linear function: $U_{2,0} = A_{2,0} + B_{2,0}y$. The upper boundary condition requires $A_{2,0} = -B_{2,0}$, allowing us to write $U_{2,0} = A_{2,0}(1-y)$. The lower boundary condition sets the value of this single constant $A_{2,0}$, so that

$$U_{2,0} = (1-y)\left(\frac{1 + 8e^4 - e^8}{1 - 18e^4 + e^8} + \frac{1}{4}\right).$$

The mean flux term for this component is then

$$Q_{2,0} = \int_{-1}^{1}(1-y)A_{2,0}\,dy = 2A_{2,0} = 2\left(\frac{1 + 8e^4 - e^8}{1 - 18e^4 + e^8} + \frac{1}{4}\right),$$

and total flux at second order is

$$Q_2 = \int_{-1}^{1} U_{2,0}\,dy - \cos(x)u_1(-1) - \frac{1}{2}\cos^2(x)u_0'(-1) = 2\frac{1 + 8e^4 - e^8}{1 - 18e^4 + e^8} + 1.$$

https://doi.org/10.1017/S144618112610042X Published online by Cambridge University Press

We may now solve for the mode-2 components, using the same form:

$$F_{2,2} = (2A_{2,2}(1-y)\cosh[2(1-y)] + (A_{2,2} + B_{2,2}(1-y))\sinh[2(1-y)])/\cosh(4),$$
$$G_{2,2} = (-B_{2,2}(1-y)\cosh[2(1-y)] + (B_{2,2}/2 - 2A_{2,2}(1-y))\sinh[2(1-y)])/\cosh(4).$$

Applying boundary conditions gives the two equations for $A_{2,2}$ and $B_{2,2}$.

This procedure may be automated. In general, the boundary conditions at order n are

$$u_n = -\sum_{m=1}^{n} \frac{f^m}{m!}\partial_y^m u_{n-m}. \tag{2.11}$$

The flux is expanded as $Q = \sum_{n=0}^{N} \epsilon^n Q_n$ and

$$Q_n = \int_{-1}^{1} u_n \, dy - \sum_{k=1}^{n} \frac{f^k}{k!}\partial_y^{k-1} u_{n-k}\Big|_{y=-1}. \tag{2.12}$$

We automated this task in Mathematica. This yielded large symbolic expressions for the flux, which was computable in a reasonable time up to order $O(\epsilon^{10})$, but which required a long time to compute for order $O(\epsilon^{12})$, and more so for $O(\epsilon^{14})$. The same task was then automated to give numerical solutions in Fortran. With careful numerics, this returns the bulk flux up to $O(\epsilon^N)$, where at $N = 160$ the numerics still appear stable. After that point, the high-order derivatives introduce very large coefficient values that are difficult to control accurately, although we expect that further refinements would allow increase in N.

For clarity, we present the main loop for this algorithm for $n > 2$ in Figure 2. First the boundary conditions are found for u_n and v_n, in terms of the modes up to n. The single coefficient for the mode-0 part of u is just $A_{n,0} = U_0^{BC}/2$. Then the two coefficients $A_{n,m}, B_{n,m}$ are found for each mode, using the boundary conditions for that mode, and mat is the 2×2 matrix:

$$\mathrm{mat}(m) = \begin{pmatrix} 2m + \tanh(2m) & 2\tanh(2m) \\ -2m\tanh(2m) & -2 + \tanh(2m)/m \end{pmatrix}.$$

Four new constants a, b, c, d are formed from the two coefficients $A_{n,m}, B_{n,m}$ such that $F = (a + by)\cosh(m(1-y)) + (c + dy)\sinh(m(1-y))$. This allows differentiation and integration of F and G any number of times, as simple linear transformations of a, b, c, d. These coefficients are stored for F, G and their derivatives. In fact, these derivatives involve coefficients that are multiplied by m for each succeeding derivative, which is numerically problematic. In the boundary condition calculations, however, the derivatives are divided by $m!$, so the derivative coefficients are calculated and stored with this factor. This change greatly increased the numerical stability of the program. These coefficients are then used to calculate the flux at each order n.

The helper routines in Figure 2 are as follows. The call to `get_ubc` implements equation (2.11), assembling the u boundary condition at each Fourier mode by

https://doi.org/10.1017/S144618112610042X Published online by Cambridge University Press

```
do n=3,nmax
  call get_ubc(n,nmax,F,ubc,F0,scaled_binomials)
  call get_vbc(n,nmax,G,vbc,scaled_binomials)
  F0(n)=0.5*ubc(0)
  do m=mod(n,2),n,2
    call solve_for_bc(mat,ubc(m),vbc(m),m,nmax,anm,bnm)
    a0 = real(m)*anm
    b0 = -real(m)*anm
    c0 = anm + bnm
    d0 = -bnm
    F(n,m,0,:)=(/a0,b0,c0,d0/)
    call g_from_f(F(n,m,0,:),real(m),G(n,m,0,:))
    do k=1,nmax
      call fdash(F(n,m,k-1,:),real(m),F(n,m,k,:),k)
      call fdash(G(n,m,k-1,:),real(m),G(n,m,k,:),k)
    enddo
  enddo
  call get_flux(n,nmax,flux,F,F0)
  if (mod(n,2)==0) then
    fluxvec(n/2)=flux(0)
  endif
enddo
```

FIGURE 2. The central loop of the algorithm for finding the coefficients for the ϵ expansion.

summing contributions from all lower-order solutions. The call to `get_vbc` does the same for v. Boundary conditions are solved using `solve_for_bc`, which solves the 2×2 system $\mathrm{Mat}(m)(A_{n,m}, B_{n,m})^T = (U^{bc}_{n,m}, V^{bc}_{n,m})^T$ to find the two free constants in $U_{n,m}$ that satisfy the boundary condition at $y = -1$. The $V_{n,m}$ coefficients are derived from the $U_{n,m}$ coefficients in `g_from_f` via the incompressibility constraint. All derivatives of F and G are computed in coefficient space using the `fdash` routine up to the highest order required. Finally, the flux is calculated using `get_flux`, which implements equation (2.12).

With $f = \cos x$, the boundary condition (2.11) may be projected onto each Fourier mode m by expanding $f^k \cos(m'x)$ as a sum of $\cos(mx)$ terms. Using the identity

$$\cos^k(x) = 2^{-(k+1)} \sum_{j=0}^{k} \binom{k}{j} \cos((k-2j)x),$$

we have

$$\cos^k(x)\cos(m'x) = \sum_{m=0}^{\infty} C(k, m', m)\cos(mx),$$

where the coefficients $C(k, m', m)$ are obtained by collecting terms with the same argument. The boundary condition for each Fourier mode m of u_n then becomes

$$U^{bc}_{n,m} = -\sum_{k=1}^{n-1} \sum_{m'=1}^{n-k} \frac{1}{k!} \partial_y^k U_{n-k,m'} \Big|_{y=-1} C(k, m', m),$$

https://doi.org/10.1017/S144618112610042X Published online by Cambridge University Press

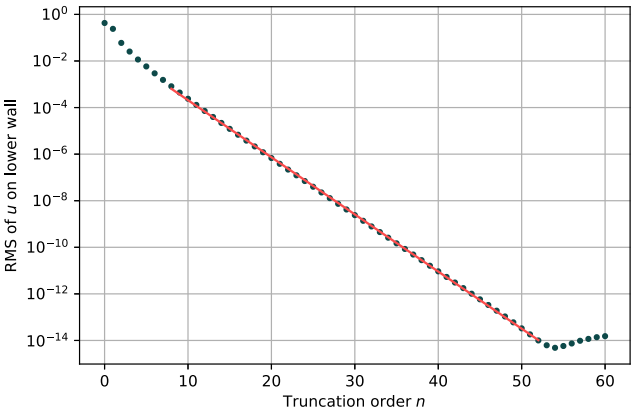


FIGURE 3. The average RMS of the velocity component u on the lower wall as a function of order n, shown with blue dots. The lower boundary parameter was fixed at $\epsilon = 0.3$. The series shows exponential convergence down to the double-precision floor near $n = 53$, beyond which a small amount of floating-point noise accumulates. A linear fit to the central data points is shown as a red line, suggesting that the RMS error decays as $\exp(-0.565n)$.

and analogously for $V^{bc}_{n,m}$, with $\cos(m'x)$ replaced by $\sin(m'x)$ in the product with f^k. `scaled_binomials` stores the precomputed coefficients for this sum. It holds the required values $S(m,j) = 2^{-(m+1)}\binom{m}{j}$.

Finally, we note that the parity constraint on the modes `do m=mod(n,2),n,2`, that is, at order n only modes of the same parity contribute, is a consequence of $f = \cos(x)$ containing a single Fourier mode. This constraint simplifies the computation in our case, but would not be appropriate for a more general boundary. The `Fortran` code is available on reasonable request to the first author.

All calculations are performed in coefficient space, making the routine very fast. For comparison, on a single-thread on an i7-7700K CPU, with $N\max = 180$, the program took less than a second at double precision, which gave numerically sensible results out to $O(\epsilon^{60})$. At quad precision, the program took just under 10 seconds, and gave numerically sensible results out to $O(\epsilon^{160})$.

The convergence of the series is demonstrated in Figure 3, which shows the average root-mean-square (RMS) value of u on the boundary for the series solution truncated at order n. In this case, we chose $\epsilon = 0.3$, and used double-precision reals. The residual decays exponentially with truncation order, as expected for a convergent power series. After the initial points, a least-squares fit to our results showed that the error behaves as $RMS_{\text{error}} \approx \exp(-0.565n)$, and this is drawn using a red line in Figure 3.

A quiver plot is shown in Figure 4, showing this convergence at the lowest orders. At $n = 0$, the flow is pure Poiseuille, passing straight through the lower wall. As each higher-order term is added, the flow is progressively adjusted in the channel and in the nonphysical region below the wall to enforce the no-slip condition.

https://doi.org/10.1017/S144618112610042X Published online by Cambridge University Press

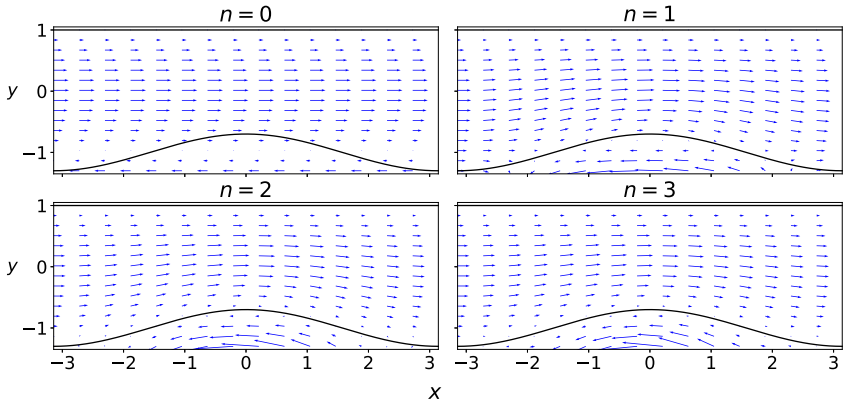


FIGURE 4. Quiver plots of the velocity field for the series truncated at orders $n = 0, 1, 2, 3$, showing the adjustment of the flow to correctly match the no-slip condition on the wavy wall. The lower boundary parameter was again fixed at $\epsilon = 0.3$. The flow field for $n > 3$ is visually identical to the $n = 3$ plot.

3. Numerical solution of the Stokes equations

We seek an accurate numerical solution for the steady Stokes equations to compare with the very high-order expansions of the previous section. We start by using spectral basis functions that meet the boundary conditions precisely. This is the no-slip-Chebyshev (NSC) basis described by the current authors [15]. Also, we incorporate the conformally mapped equations described there, but with the nonlinear (inertial) terms removed. The steady Stokes equations are numerically stiff, but linear, so we choose to solve the large matrix equations using the generalised minimal residual (GMRES) method [9], to avoid storing and manipulating very large matrices.

In summary, the numerical method uses a periodic Fourier basis in x and an NSC basis in y, a stream function to assert incompressibility, and a numerical conformal mapping to map the system to a rectangular computational region. A GMRES method is used with the residual forced below 10^{-10}, ensuring that the linear system was solved to high accuracy at each grid resolution. Grid convergence was then assessed by comparing the bulk flux Q across successive refinements (Tables 1 and 2). For $\epsilon < 1.5$, convergence is rapid, agreeing with the results from coarser grids to at least four significant figures. For higher values of ϵ, the results are converged to at least one significant figure with a 512×512 grid. For maximum $\epsilon = 1.95$, approaching the pinch-off limit $\epsilon \to 2$, the numerical solver struggles at lower grid resolutions, but comparing the 512×512 results with a longer run on a 768×768 grid, we found that the results agreed with the 512×512 results to two significant figures, $Q = 2.7 \times 10^{-4}$ on both 512 and 768 grids. We consider this level of accuracy sufficient for comparison with the series expansion.

First the numerical conformal mapping was performed for $\epsilon = 0$ to $\epsilon = 1.95$ in steps of 0.05. The mapped lower wall location was compared with the analytic function $y = -1 + \epsilon \cos x$, and the grid refined until agreement was satisfactory. For the

https://doi.org/10.1017/S144618112610042X Published online by Cambridge University Press

TABLE 1. Grid convergence of bulk flux Q at $\epsilon = 1.50$. Each row shows the change relative to the previous refinement level.

Resolution	Q	$\lvert Q - Q_{\text{prev}}\rvert$	$\lvert Q - Q_{\text{prev}}\rvert/\lvert Q_{\text{prev}}\rvert$
256×256	0.105 171 15	–	–
384×384	0.105 801 75	6.31×10^{-4}	6.00×10^{-3}
448×448	0.105 824 54	2.28×10^{-5}	2.15×10^{-4}
480×480	0.105 827 74	3.20×10^{-6}	3.03×10^{-5}
512×512	0.105 829 18	1.44×10^{-6}	1.36×10^{-5}

TABLE 2. Grid convergence of bulk flux Q at $\epsilon = 1.75$. Higher grid refinement is needed for convergence of results in this very constricted channel.

Resolution	Q	$\lvert Q - Q_{\text{prev}}\rvert$	$\lvert Q - Q_{\text{prev}}\rvert/\lvert Q_{\text{prev}}\rvert$
256×256	0.013 981 42	–	–
384×384	0.019 544 47	5.56×10^{-3}	3.98×10^{-1}
448×448	0.020 622 83	1.08×10^{-3}	5.52×10^{-2}
480×480	0.020 962 59	3.40×10^{-4}	1.65×10^{-2}
512×512	0.021 215 05	2.52×10^{-4}	1.20×10^{-2}

mapping code, a 3200×3200 grid was used, generating 2400 mapping coefficients. At this resolution, the absolute maximum difference was near machine precision (10^{-12}) up to $\epsilon = 1.6$, dropping to 8×10^{-4} for $\epsilon = 1.95$. For each value of ϵ, the 2400 coefficients that determine the mapping were stored to disk to be used by the GMRES Stokes solver. For the 40 values of ϵ these mappings took 420 minutes to complete (roughly 10 minutes each).

4. Comparison of results

The purely numerical results (stars) are compared with the results of the perturbation expansion at various orders (dashed-dotted lines) in Figure 5. At the lowest approximation, $O(\epsilon^2)$, the perturbation expansion agrees with the numerical data up to $\epsilon \approx 0.25$. The higher-order terms improve this agreement up to $\epsilon = 0.9$. However, near $\epsilon = 0.95$, the series appears to diverge for all orders, the highest shown being $O(\epsilon^{180})$. Therefore, diagonal Padé approximants were formed from the coefficients in order to model the flux beyond that point. These approximants are shown with solid lines. It may be seen that all the Padé approximants higher than the [3/3] visually match the numerical results.

Padé approximants $[m/n]$ are rational functions involving the first $m + n + 1$ coefficients of a power series, whose Maclaurin expansion agrees with the original power series to order $m + n$. Full details may be found in Baker and Graves-Morris [2].

https://doi.org/10.1017/S144618112610042X Published online by Cambridge University Press

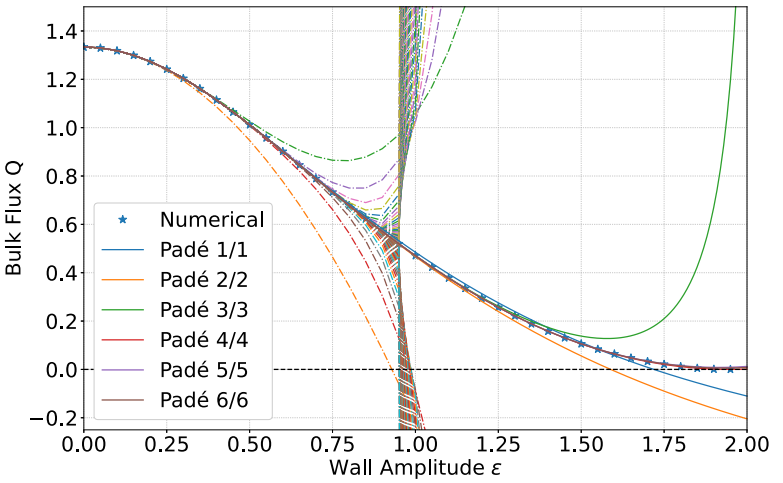


FIGURE 5. The bulk flux at various amplitudes of the lower wall function, from straight channel ($\epsilon = 0$) to the point where the lower wall amplitude is just large enough to pinch off the opening ($\epsilon = 2$). The stars are the numerical results, for $\epsilon = 0, 0.05, 0.1, \cdots, 1.95$. The dashed-dotted lines are the results of the perturbation expansion, diverging near $\epsilon = 0.95$, with the highest-order results being the steepest at that point. The solid lines are the first six diagonal Padé approximants, based on the perturbation coefficients. The [4/4] to [6/6] approximants are visually indistinguishable.

The lowest-order Padé approximant uses the three lowest coefficients from the series c_0, c_1, c_2 in the form

$$\begin{aligned}
c_0 &= 4/3, \\
c_1 &= -\frac{-3 + 2e^4 + e^8}{1 - 18e^4 + e^8} \approx -1.544\,201\,551\,917\,25, \\
c_2 &= \frac{n_{11}}{d_{11}} \approx 1.265\,778\,229\,812\,035, \\
n_{11} &= -45 + 1012e^4 + 15\,572e^8 + 26\,284e^{12} - 4566e^{16} \\
&\quad - 1652e^{20} - 3804e^{24} - 44e^{28} + 11e^{32}, \\
d_{11} &= 16(1 - 18e^4 + e^8)^2(1 - 66e^8 + e^{16}), \\
Q_{11} &= \frac{c_0c_1 + (c_1^2 - c_0c_2)\epsilon^2}{c_1 - c_2\epsilon^2} \approx \frac{2.058\,935\,4 - 0.696\,854\epsilon^2}{1.544\,202 + 1.265\,778\epsilon^2}.
\end{aligned}$$

Even this simple ratio is surprisingly accurate, visually matching the numerical results up to about $\epsilon = 0.75$. At higher orders, the form of the exact coefficients quickly becomes unwieldy, but they can always be approximated by their numerical values to 16 significant figures as

$$\begin{aligned}
c_3 &\approx -1.145\,261\,858\,484\,969, \\
c_4 &\approx 1.114\,570\,034\,610\,418.
\end{aligned} \tag{4.1}$$

https://doi.org/10.1017/S144618112610042X Published online by Cambridge University Press

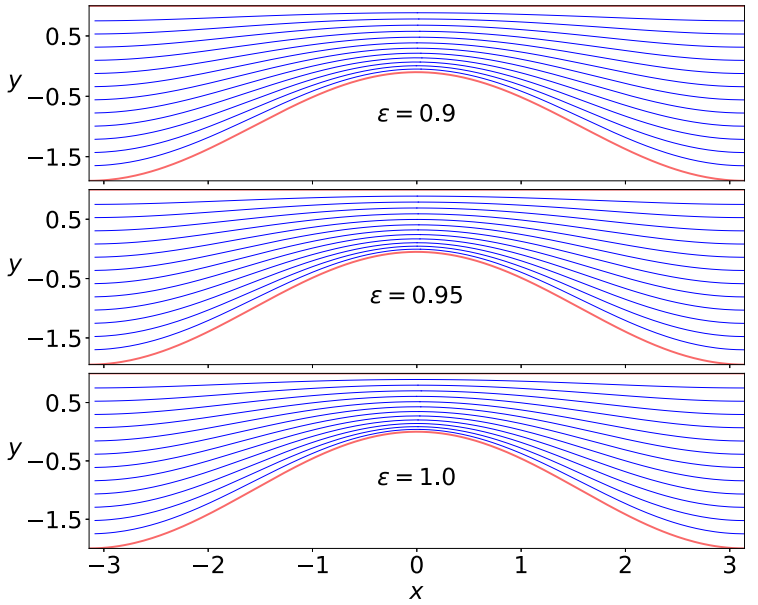


FIGURE 6. Streamlines for values of ϵ near 0.95, where the perturbation series diverges. The flow appears largely unchanged, indicating that the divergence is not related to any physical mechanism.

The [2/2] approximant uses the first five coefficients $(c_0, c_1, c_2, c_3, c_4)$ in the form

$$\begin{aligned} n_{22} &= c_0(c_2^2 - c_1c_3) + (c_1(c_2^2 - c_1c_3) + c_0(c_1c_4 - c_2c_3))\epsilon^2 \\ &\quad + (c_0(c_3^2 - c_2c_4) + c_1(c_1c_4 - c_2c_3) + c_2(c_2^2 - c_1c_3))\epsilon^4, \\ d_{22} &= c_2^2 - c_1c_3 + (c_1c_4 - c_2c_3)\epsilon^2 + (c_3^2 - c_2c_4)\epsilon^4, \\ Q_{22} &= \frac{n_{22}}{d_{22}} \approx \frac{0.221\,761 + 0.105\,132\epsilon^2 - 0.076\,452\,7\epsilon^4}{0.166\,321 + 0.271\,473\epsilon^2 + 0.099\,173\,8\epsilon^4}. \end{aligned} \tag{4.2}$$

From Figure 5, we see that this is visually accurate up to about $\epsilon = 1.1$. Each Padé approximant is found by solving a small linear system involving the coefficients. By the time we have the [4/4] approximant, the results visually match the numerical results. Higher-order Padé approximants ($n > 4$) agree very closely with the lower-order approximants and numerical results, with the higher-order approximants giving some small gains near $\epsilon = 2$, where the flux should be zero (the channel is pinched shut at $\epsilon = 2$). These Padé approximants ameliorate the divergence of the series at $\epsilon = 0.95$, and are a very effective way to accurately approximate the bulk flux with very little computation time.

There is no obvious physical reason why the series diverges near $\epsilon = 0.95$. In Figure 6, the streamlines are plotted from the numerical data for wall amplitude $\epsilon = 0.9, 0.95, 1$. Apart from the small change in the wall shape, the flow may be seen to remain largely the same in each panel, showing no recirculation zones or topological

https://doi.org/10.1017/S144618112610042X Published online by Cambridge University Press

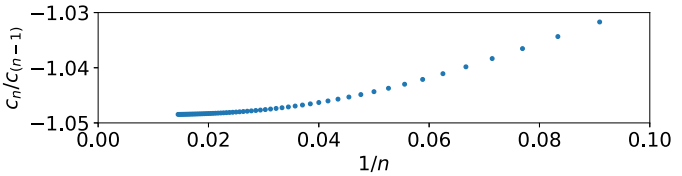


FIGURE 7. A Domb–Sykes plot of the ratios of the coefficients of the power series in ϵ^2 against $1/n$. The ratios are converging near −1.0485.

changes across the divergence threshold, indicating that there is no obvious physical mechanism for the divergence of the perturbation expansion near $\epsilon = 0.95$.

To investigate this further, we present a Domb–Sykes plot [4] in Figure 7. This shows the ratio of the coefficients c_n/c_{n-1} plotted against $1/n$. The rationale for this is that for a series $\sum c_n\epsilon^{2n}$, the ratio c_n/c_{n-1} converges to $1/\epsilon_c^2$, where ϵ_c^2 is the radius of convergence. The first ten points have been excluded while the series settles down, leaving the ratios for coefficients of ϵ^{20} to ϵ^{160}. It is apparent that the ratios are still not in the linear regime, but it may be seen that the curve will cross the axis somewhere near −1.0485. This suggests a singularity near $\epsilon^2 \approx -1/1.0485 \approx -0.95$. This shows good agreement with the divergence of the series, seen in Figure 5 near $\epsilon \approx \sqrt{0.95} \approx 0.97$.

Van Dyke [14] and Domb and Sykes [4] argue further that both the intercept and slope of the Domb–Sykes plot yield information about the radius of convergence and the nature of the nearest singularity. In order to study these further, we next applied Aitken's Δ^2 extrapolation method [1] on the ratio data in an attempt to clarify the intercept and slope of the Domb–Sykes plot. We define the sequence of ratios $S_n = c_n/c_{(n-1)}$ and seek to estimate its limit as $n \to \infty$. To estimate this limit, the Aitken transform computes a new sequence as

$$S_n^E = \frac{S_{n+1}S_{n-1} - S_n^2}{S_{n+1} - 2S_n + S_{n-1}}.$$

The extrapolated terms S_n^E form a new sequence with two fewer terms. This procedure may be repeated with the new sequence S^E. Five such extrapolations were performed and a linear fit applied to the last ten points to give an estimate of the intercept and slope at each level. The results are shown in Table 3 both for the original coefficient ratios, and also after extrapolation up to five times. The intercept appears to stabilise after only two extrapolations.

For a singularity of the form $(\epsilon^2 + \epsilon_c^2)^\alpha$, the coefficient ratio has the form $c_n/c_{n-1} \sim (1/\epsilon_c^2)(1 - (1+\alpha)/n)$ so that the Domb–Sykes plot has a slope proportional to $\alpha + 1$. The zero slope suggested by the data in Table 3 would imply $\alpha = -1$: a simple pole. This pole is located approximately at $\epsilon^2 = -1/1.048\,51 = -0.953\,73$, closely matching the visual estimate of the intercept and a zero in each of the Padé denominators. This also agrees well with the apparent radius of convergence limitation apparent in Figure 5. In terms of ϵ the singularity is therefore on the imaginary axis at

https://doi.org/10.1017/S144618112610042X Published online by Cambridge University Press

TABLE 3. Intercept and slope for the coefficient ratio data. The first column i indicates the number of repeated Aitken extrapolations used. The intercept appears stable after two extrapolations.

i	intercept	slope
0	−1.048 762 0	0.020 794 7
1	−1.048 537 2	0.002 162 1
2	−1.048 508 1	−0.000 013 8
3	−1.048 506 5	−0.000 104 9
4	−1.048 511 2	0.000 183 2
5	−1.048 513 1	0.000 292 9

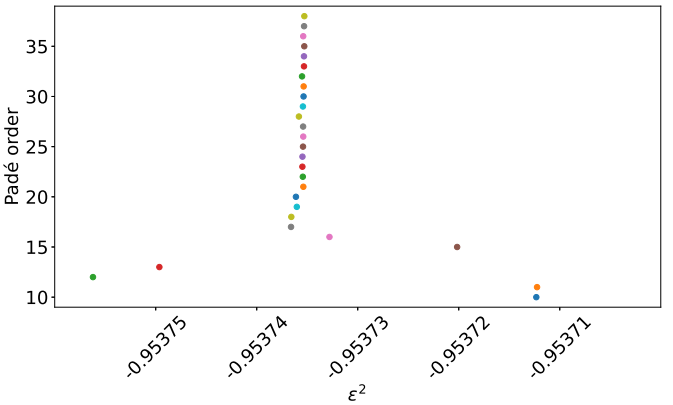


FIGURE 8. The Padé poles near $\epsilon^2 = -0.95$, shown for Padé approximants from [10/10] to [38/38]. These converge near −0.953 735 3.

$\pm\sqrt{0.954}i \approx \pm 0.977i$. This suggests that the divergence of the series is not connected to any geometric feature of the physical channel, but reflects the analytic structure in the complex ϵ plane. Mathematically, therefore, the series (2.3) close to the nearest singularity behaves as $(\epsilon - 0.977i)^{-1}(\epsilon + 0.977i)^{-1} = (\epsilon^2 + 0.954)^{-1}$.

In addition to the visual inspection of the Domb–Sykes plot, and the use of Aitken extrapolation, a third check to locate the singularity is to investigate the zeros of the Padé approximants. We did this using the root-finding function for polynomials in the Python library `numpy`. We found that the denominator in each fraction has a zero near −0.95. As the order of the approximants increases, these zeros converge to approximately −0.953 735 3, shown in Figure 8. This agrees with the results of the Aitken extrapolation to five significant figures, providing strong support for this being the location of the singularity.

We now present a comparison with lubrication theory (LT). By converting the domain to $\epsilon/2(1 + \cos(x)) < y < 1$, we can compare directly with the results of Tavakol *et al.* [13]. To do so, we have converted our results from flux at constant pressure

https://doi.org/10.1017/S144618112610042X Published online by Cambridge University Press

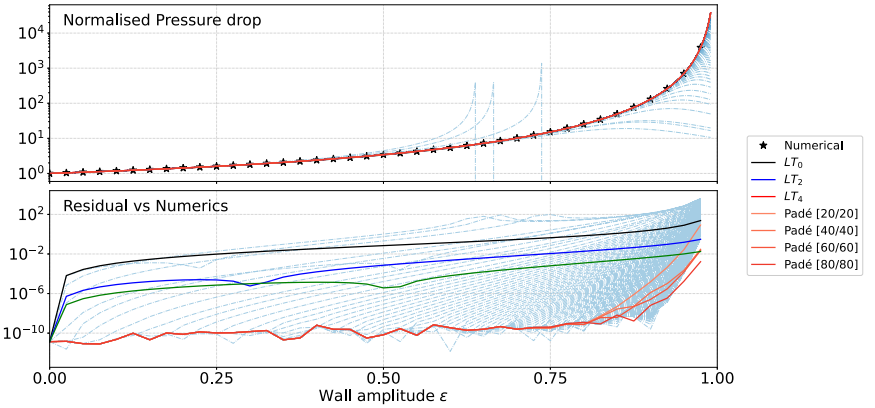


FIGURE 9. Comparison of pressure drop with lubrication theory (LT) in a channel with lower wall at $y = \epsilon/2(1 + \cos x)$ and upper wall at $y = 1$. The upper plot shows the numerical results (stars) with the perturbation expansion (light blue dashed lines) at order $O(\epsilon^1)$ to $O(\epsilon^{160})$, the lubrication theory and its first and second corrections, and [20/20], [40/40], [60/60], [80/80] Padé approximants. In the lower plot, the residuals (difference with numerics) are shown. Kinks in the LT plots are due to points where the residual changes sign.

gradient to pressure drop for constant flux, via the relation $\Delta P_x/P_x = Q_0/Q_{\text{numerical}}$. This relation holds in the Stokes flow linear regime, where the flux is linearly proportional to the pressure gradient. The new domain includes a zeroth-order term in the lower boundary, as well as the first-order term, so the expansion must now include all modes up to order n, not just those of the same parity. These changes mean that there are flux terms at all integer powers of ϵ, not just even powers.

With a significant amount of algebra, the bulk flux for this channel geometry was calculated by hand in a similar way to Section 2 out to order $O(\epsilon^2)$, and found to be

$$Q = \frac{1}{6} - \frac{\epsilon}{4} + \frac{\epsilon^2}{4}\left(1 - \frac{2 - \sinh(2)}{4(1 - \sinh^2(1))}\right) + O(\epsilon^3)$$

The series was then expanded numerically to order ϵ^{160}, and Padé approximants formed from the coefficients. The upper plot in Figure 9 shows the pressure drop as ϵ goes from 0 (straight wall) to 1 (channel pinched shut). The numerical solution is shown with stars. We see that the higher-order terms bring the perturbation expansion ever closer to the numerical solution, while the higher-order Padé approximants and the LT results are visually identical with the numerical solution.

The lower frame in Figure 9 shows the difference between the approximations and the numerical solution. The absolute value of this residual is plotted using a log scale. We see that the expansion is better for small ϵ, even at low order in ϵ, whereas the LT approximation is quite good even for high values of ϵ, and clearly improves as the correction terms are added. At the highest value of ϵ used in the numerical method (0.975), the perturbation expansion requires terms at order ϵ^{80} to match the standard

https://doi.org/10.1017/S144618112610042X Published online by Cambridge University Press

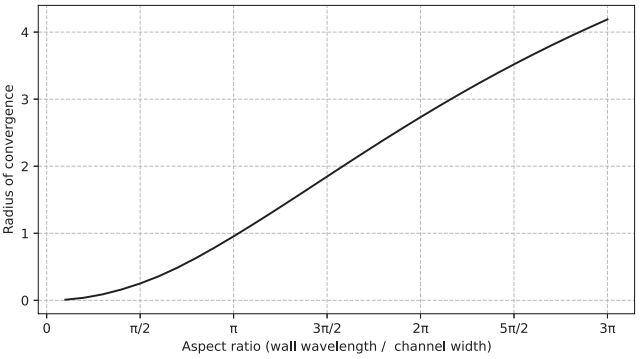


FIGURE 10. The effect of channel aspect ratio on radius of convergence of the series. The curve crosses the physically meaningful channel pinch-off point of $R = 2$ near 1.6π. For larger aspect ratios the series will converge for all physically sensible wall amplitudes.

LT method, and at order ϵ^{160} to match the first correction to LT, $O(\delta^2)$, where δ is the maximum-width-to-half-wavelength aspect ratio, in this case $1/\pi$. Note the difference to our earlier definition of aspect ratio, which was wavelength to mean width. The reason such high-order terms are required here is that the error decays only as ϵ^n near the radius of convergence. However, the Padé approximants are again very effective in increasing the accuracy. The [20/20] approximant beats the LT approximation at $\epsilon = 0.975$, and the [40/40] matches the second correction to LT $O(\delta^4)$. The [80/80] approximant is significantly more accurate than all other methods shown here.

Note that in this formulation we do not encounter an analytic singularity within the physical regime, as we did in Figure 5. Instead the ratio of the coefficients converges to 1, corresponding to the expected physical pinch-off of the channel, explaining the slow convergence of the perturbation series as ϵ approaches 1.

We conclude this section with an investigation into the effect of aspect ratio on the radius of convergence of the series. Reverting to our definition of aspect ratio as the wavelength divided by the mean channel width, the main study has been on a channel with aspect ratio π. Keeping the mean channel width $-1 < y < 1$, the wavelength has been varied as $-\alpha\pi < x < \alpha\pi$ and the lower wall is at $y = -1 + \epsilon\cos(\alpha x)$. Varying the value of α from 0.1 to 3, the radius of convergence was estimated from the asymptotic ratio of successive series coefficients, and then plotted in Figure 10. Note that once the radius of convergence is greater than 2, it is beyond the physical range, which should allow the series to converge for all physically meaningful values of the wall amplitude.

5. Conclusion

This paper presents a high-order perturbation expansion for the bulk flux through a 2D channel with a sinusoidal lower wall and a flat upper wall. The perturbation is carried out numerically to $O(\epsilon^{160})$, where ϵ is the amplitude of the lower

https://doi.org/10.1017/S144618112610042X Published online by Cambridge University Press

wall undulation. A numerical method is used as a check, and the agreement with the expanded series is excellent, until the radius of convergence is reached near $\epsilon \approx 0.97$.

Diagonal Padé approximants from [1/1] to [15/15] are formed to proceed past the $\epsilon \approx 0.97$ point, and all of these beyond [3/3] show excellent agreement with the purely numerical method at all values of ϵ. In (4.1) and (4.2), we have given all the information needed to calculate the [2/2] Padé approximant in closed form. Figure 5 shows that this simple expression already gives a reasonable approximation to the flux, and so (4.2) may be useful for engineering applications where such an approximation is required.

The nature and location of the analytic singularity was then investigated further through the use of a Domb–Sykes plot, and with the use of Aitken's Δ^2 method. The singularity appears to be due to simple poles in the complex ϵ plane near $\pm 0.977i$. A brief investigation of the effect of aspect ratio on the location of this singularity was pursued, and it was found that when the wall wavelength is greater than the channel width by a factor of about 1.6π, the singularity has moved outside the physically relevant region.

Finally, a comparison with lubrication theory is presented, with diagonal Padé approximants of order [80/80] being found to be much more accurate than all other methods used here, for all values of ϵ tested.

This work might easily be extended in terms of generalising the channels studied. As the approach breaks the velocities into Fourier modes, it would not be difficult to modify the procedure for the case of any smooth periodic wall shape, by Fourier analysis and treatment of each mode in the wall undulation. In the comparison with Tavakol *et al*. [13] in Section 4, we did generalise the expansion to deal with a lower boundary having both a zero mode and a mode-1 component.

More involved extensions would include the case of both walls undulating, and the reintroduction of inertial terms to go beyond pure Stokes flow. We note that until now we have only dealt with smooth boundary shapes, and further study would be required to determine whether the method can be suitably adapted to boundaries with discontinuous derivatives.

Timing estimates are provided for calculation of flux through the channel. Our numerical method calculated the steady flow for each of the 40 values of ϵ. We have not investigated other numerical methods, and it may be that there are methods that can produce similar or better accuracy in a shorter time. Our purely numerical procedure, using a GMRES solver with conformal mapping for the 40 values of ϵ, gave sufficiently accurate results in approximately 14 hours; 7 hours were needed to sequentially build up the conformal maps, and another 7 hours to solve the steady-state problem for each value of ϵ. In contrast, the perturbation expansion and Padé approximants took only 10 seconds, covering the entire physical range $0 < \epsilon < 2$. This perturbation approach therefore provides a vastly more efficient way to determine the effect on flow past sinusoidal undulations in a wall of a 2D channel, and reveals an interesting underlying singularity structure not apparent in the purely numerical approach.

https://doi.org/10.1017/S144618112610042X Published online by Cambridge University Press

Acknowledgement

The authors thank two anonymous reviewers for their suggestions that have enabled us to significantly improve and extend the material in this paper.

References

[1] A. Aitken, "On Bernoulli's numerical solution of algebraic equations", *Proc. Roy. Soc. Edinburgh* **46** (1926) 289–305; doi:10.1017/S0370164600022070.

[2] G. A. Baker and P. Graves-Morris, *Padé approximants* (Cambridge University Press, Cambridge, 1996).

[3] W. Coenen, X. Zhang and A. L. Sanchez, "Lubrication analysis of peristaltic motion in non-axisymmetric annular tubes", *J. Fluid Mech.* **921** (2021) R2; doi:10.1017/jfm.2021.525.

[4] C. Domb and M. F. Sykes, "On the susceptibility of a ferromagnetic above the Curie point", *Proc. R. Soc. Lond.* **240** (1957) 214–228; doi:10.1098/rspa.1957.0078.

[5] J. B. Freund and M. M. Orescanin, "Cellular flow in a small blood vessel", *J. Fluid Mech.* **671** (2011) 466–490; doi:10.1017/S0022112010005835.

[6] A. E. Malevich, V. V. Mityushev and P. M. Adler, "Stokes flow through a channel with wavy walls", *Acta Mech.* **182**(3) (2006) 151–182; doi:10.1007/s00707-005-0293-4.

[7] C. Pozrikidis, "Creeping flow in two-dimensional channels", *J. Fluid Mech.* **180** (1987) 495–514; doi:10.1017/s0022112087001927.

[8] O. Reynolds, "On the theory of lubrication and its application to Mr. Beauchamp tower's experiments, including an experimental determination of the viscosity of olive oil", *Philos. Trans. R. Soc.* **177** (1886) 157–234; doi:10.1098/rstl.1886.0005.

[9] Y. Saad, "A generalized minimal residual algorithm for solving nonsymmetric linear systems", *SIAM J. Sci. Stat. Comput.* **7** (1986) 417–424; doi:10.1137/0907058.

[10] E. A. Saibel and N. A. Macken, "The fluid mechanics of lubrication", *Annu. Rev. Fluid Mech.* **5**(1) (1973) 185–212; doi:10.1146/annurev.fl.05.010173.001153.

[11] I. J. Sobey, "On flow through furrowed channels. Part 1. Calculated flow patterns", *J. Fluid Mech.* **96**(1) (1980) 1–26; doi:10.1017/s002211208000198x.

[12] S. Tsangaris and E. Leiter, "On laminar steady flow in sinusoidal channels", *J. Engrg. Math.* **18**(2) (1984) 89–103; doi:10.1007/bf00042729.

[13] B. Tavakol, G. Froehlicher, D. P. Holmes and H. A. Stone, "Extended lubrication theory: improved estimates of flow in channels with variable geometry", *Proc. R. Soc. A* **473** (2017) 20170234; doi:10.1098/rspa.2017.0234.

[14] M. Van Dyke, "Analysis and improvement of perturbation series", *Quart. J. Mech. Appl. Math.* **27**(4) (1974) 423–450; doi:10.1093/qjmam/27.4.423.

[15] S. J. Walters and L. K. Forbes, "A global spectral method for wavy channel flow in 2D", *ANZIAM J.* **68** (2026) e7; doi:10.1017/S1446181126100327.

https://doi.org/10.1017/S144618112610042X Published online by Cambridge University Press